ADVANCED OPTICAL MATERIALS
www.advopticalmat.de

Stacked Dual-Wavelength Near-Infrared Organic Photodetectors

Yazhong Wang, Bernhard Siegmund, Zheng Tang, Zaifei Ma, Jonas Kublitski, Shen Xing, Vasileios C. Nikolis, Sascha Ullbrich, Yungui Li, Johannes Benduhn, Donato Spoltore, Koen Vandewal,* and Karl Leo*

Organic near-infrared (NIR) detectors have potential applications in biomedicine, agriculture, and manufacturing industries to identify and quantify materials contactless, in real time and at a low cost. Recently, tunable narrow-band NIR sensors based on charge-transfer state absorption of bulk-heterojunctions embedded into Fabry-Pérot micro-cavities have been demonstrated. In this work, this type of sensor is further miniaturized by stacking two sub-cavities on top of each other. The resulting three-terminal device detects and distinguishes photons at two specific wavelengths. By varying the thickness of each sub-cavity, the detection ranges of the two sub-sensors are tuned independently between 790 and 1180, and 1020 and 1435 nm, respectively, with full-width-at-half-maxima ranging between 35 and 61 nm. Transfer matrix modeling is employed to select and optimize device architectures with a suppressed cross-talk in the coupled resonator system formed by the sub-cavities, and thus to allow for two distinct resonances. These stacked photodetectors pave the way for highly integrated, bi-signal spectroscopy tunable over a broad NIR range. To demonstrate the application potential, the stacked dual sensor is used to determine the ethanol concentration in a water solution.

1. Introduction

Organic photodetectors (OPDs) have intrinsic advantages such as light-weight, low cost, high scalability and bio-compatibility, which can be well employed for producing wearable, flexible and cost-effective spectroscopic sensors.[1,2] Special focus has been laid on OPDs capable of detecting the near infrared (NIR) spectral region due to many important applications, such as temperature monitoring, food quality testing, ingredient analyzing, and night vision.[3–6]

Spectroscopic detection and narrow-band OPDs can be achieved by employing optical filters, dichroic prisms, or gratings with broadband photodetectors.[7] Alternatively, methods including optical thick junctions for charge narrowing collection[8–10] or new polymeric or molecular materials with tailored sharp absorption peaks in the NIR have been used.[11,12] The above detector concepts, however, have drawbacks such as complicated device architectures or a limited tunability of the detection range. To overcome these problems, a Fabry–Pérot resonance micro-cavity[13] device architecture, where the resonance wavelength is tuned within the weakly absorbing charge-transfer (CT) state absorption band[14] of the organic photo-active donor–acceptor blend has been recently introduced.[15,16] This novel class of

Y. Wang, J. Kublitski, S. Xing, Dr. J. Benduhn, Dr. D. Spoltore, Prof. K. Leo
Dresden Integrated Center for Applied Physics and Photonic Materials (IAPP) and Institute for Applied Physics
Technische Universität Dresden
Nöthnitzer Str. 61, 01187 Dresden, Germany
E-mail: yazhong.wang@tu-dresden.de

Dr. B. Siegmund, V. C. Nikolis
Heliatek GmbH
Treidlerstraße 3, 01139 Dresden, Germany

The ORCID identification number(s) for the author(s) of this article can be found under https://doi.org/10.1002/adom.202001784.

DOI: 10.1002/adom.202001784

Prof. Z. Tang, Prof. Z. Ma
Center for Advanced Low-dimension Materials
State Key Laboratory for Modification of Chemical Fibers and Polymer Materials
College of Materials Science and Engineering
Donghua University
Renmin North Road 2999, Shanghai 201620, P. R. China

S. Ullbrich
Senorics GmbH
Räcknitzhöhe 35, 01217 Dresden, Germany

Dr. Y. Li
Max-Planck Institute for Polymer Research
Ackermannweg 10, 55128 Mainz, Germany

Prof. K. Vandewal
Institute for Materials Research (IMO-IMOMEC)
Hasselt University
Wetenschapspark 1, Diepenbeek 3590, Belgium
E-mail: koen.vandewal@uhasselt.be

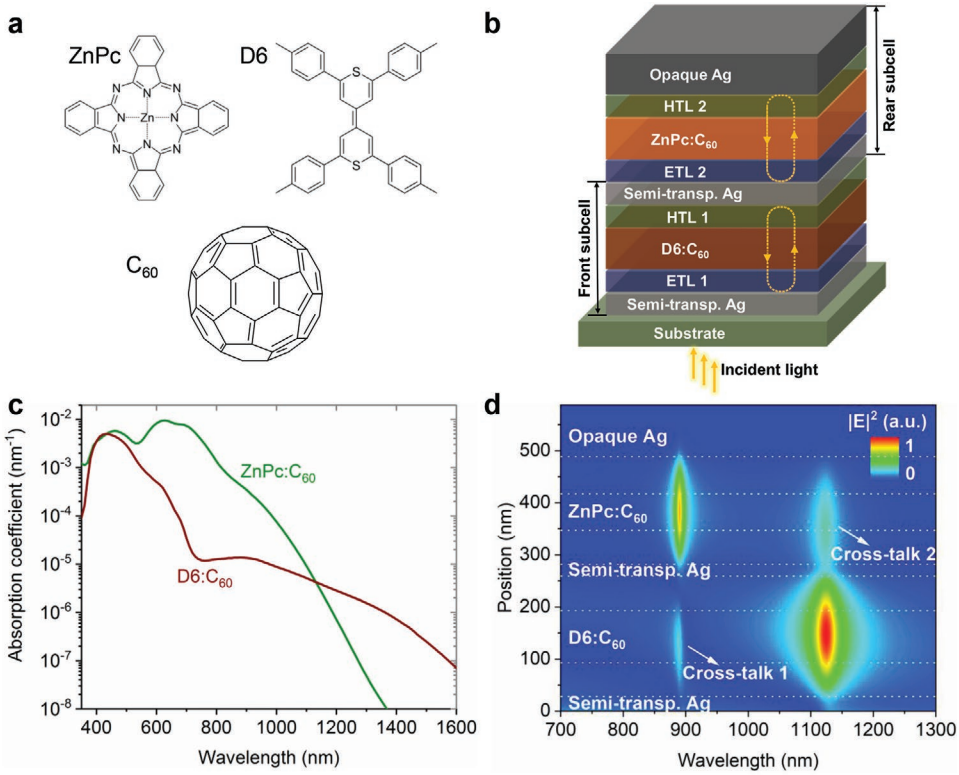

Figure 1. a) Chemical structure of the BHJ components: ZnPc, D6 and C_{60}. b) Simplified device architecture of the stacked dual wavelength NIR OPDs. Two sub-cavities are formed by three Ag mirrors/electrodes. Light incident from the glass substrate. c) Absorption coefficients of ZnPc:C_{60} (1:1, wt%), D6:C_{60} (5:95, wt%). d) Simulated electromagnetic field distribution in the stacked cavity enhanced photodetector. To achieve the maximum responses at the resonance wavelengths, the thicknesses of photo-active layers ZnPc:C_{60} and D6:C_{60}, are tuned to locate them in the maximum of the corresponding optical field.

OPDs allows to reliable identify and quantify substances contactless and in real-time, based on their characteristic absorption peaks in the NIR. To further miniaturize these sensors, it is desirable to detect and distinguish several wavelengths via a single detecting surface.[17,18] Hereby, the accuracy of substance identification improves with the number of wavelengths detected. For example, signal ratios for two wavelengths will be independent of the incident light intensity. Furthermore, stacked OPDs can provide a low-cost alternative for Si-InGaAs two color detectors, typically used for remote temperature measurements. Also this type of measurement requires the ratio of radiation intensities at two wavelengths which is then compared to the blackbody radiation curve.

In this work, we realize dual wavelength detecting NIR OPDs by using thermal evaporation at ultra-high vacuum. The device consists of three silver (Ag) electrodes/mirrors, which form two sub-cavities stacked on top of each other. Within the sub-cavities, two bulk heterojunction (BHJ) blends (ZnPc:C_{60} and D6:C_{60}) are inserted and give rise to two spectral complementary CT state absorption bands, where ZnPc is zinc phthalocyanine, and D6 is 2,2′,6,6′-tetra-*p*-tolyl-4,4′-bithiopyranylidene. ZnPc and D6 are used as electron donor, while C_{60} is bulkminster fullerene and used as acceptor. Their chemical structures are shown in **Figure 1**a. Transfer matrix modeling (TMM)[19] is used to optimize thicknesses of electrodes, transport and active layers in order to maximize the absorption within the active layers at the desired resonance wavelengths, as well as to minimize optical cross-talk between the coupled subcells. We experimentally demonstrate that the resonance wavelengths of the subcells can be tuned independently within the wavelength ranges 790–1180 and 1020–1435 nm, respectively. The full-width-at-half-maxima (FWHM) of the two response wavelengths are down to 35 and 61 nm, respectively. As an example of application, we demonstrate how the dual signal sensor allows to reliably determine the ethanol concentration in water.

2. Results and Discussion

2.1. Device Architecture and Materials

The full device architecture of the stacked dual wavelength NIR OPDs is shown in Figure 1b. Two subcells are stacked sharing a common Ag electrode. Each subcell can be contacted independently via their second individual Ag electrode.[20] The absorber layer of each subcell is sandwiched between an electron transporting layer (ETL) and hole transporting layer (HTL). More detailed device architecture information can be found in Table S1, Supporting Information. The subcells form two coupled Fabry–Pérot micro-cavities for which the resonance wavelengths are proportional to the individual cavity thicknesses. Therefore, by varying the thickness of BHJ layers of each subcell, the

desired detection wavelengths can be selected. The ETL and HTL are kept at equal thickness, placing the active layer in the center of the cavity, in the maximum of the optical field.

The wavelength dependent absorption coefficient of ZnPc:C_{60} and D6:C_{60} are shown in Figure 1c. The energy of the intermolecular CT state (E_{CT}) of ZnPc:C_{60} is 1.17 eV allowing for resonance wavelengths up to 1100 nm.[21] Longer wavelength absorption is provided by the D6:C_{60} subcell, which has a more redshifted E_{CT} of 0.87 eV.[22] The energy level diagram of the involved materials in the stacked OPDs can be found in Figure S1, Supporting Information. The CT state absorption of ZnPc:C_{60} is stronger in the wavelength range 750–1100 nm, than the CT state absorption of D6:C_{60} in the range 1100–1600 nm. To compensate for this, the D6:C_{60} subcell is placed as the front subcell, that is, light passes this subcell first. The resonance wavelengths of the D6:C_{60} (ZnPc:C_{60}) containing subcell are tuned to be longer (shorter) than 1100 nm.

2.2. Optimization of the Bottom and Intermediate Mirror Thicknesses

The absorption enhancement at the resonance wavelengths in each subcell is critically controlled by the thicknesses of the semi-transparent Ag mirrors. Using TMM, we find an optimized thicknesses of intermediate and bottom, Ag mirrors to be 20 and 25 nm, respectively. The opaque Ag mirror at the back of the device is 100 nm. Further details regarding the optimized Ag mirror thicknesses are included in Figure S2, Supporting Information.

2.3. Avoiding Cross-Talk in Coupled Resonators

When stacking two micro-cavities on top of each other, undesired cross-talk resonances might occur: As the two cavities are optically coupled, a fraction of light from the resonance in the front sub-cavity is transmitted in the rear sub-cavity, and vice versa. Even though the two states are far from resonance, there is a certain delocalization over both cavities which can generate an unwanted response of one subcell at the resonance wavelength of the other subcell. In the following section, we describe how to successfully minimize this effect.

Figure 1d illustrates the simulated electromagnetic field distribution within the stacked photodetector. Besides the desired resonance wavelength of 890 nm in the ZnPc:C_{60} rear cell, a smaller, undesired peak at 1120 nm (labeled as cross-talk 2) is present and related to the front cell resonance. Similarly, we observe an undesired resonance at 890 nm (labeled as cross-talk 1) in the D6:C_{60} front cell, together with a large enhancement at the desired wavelength of 1120 nm. Using a series of TMM optical simulations, we find the optimum position and thickness of photo-active layers within the cavity where the influence of electromagnetic field enhancement at the undesired wavelengths is minimized. This optimized device architecture is shown in Figure 1d.

The strategy we followed to suppress the above described cross-talk is to combine photo-active materials with complementary absorption coefficients at the desired resonance wavelengths. The absorption coefficient of ZnPc:C_{60} is much larger (20–100 times) than that of D6:C_{60} at the desired resonance wavelengths. We therefore place the D6:C_{60} subcell in the front, and adjust the active layer thickness to achieve resonance wavelength between 1100 and 1435 nm. The ZnPc:C_{60} subcell placed in the back has its resonance frequency tuned to shorter wavelengths (750–1100 nm). The undesired coupled resonance at 1100–1435 nm in the ZnPc:C_{60} cell is barely visible, since ZnPc:C_{60} contains no significant CT state (or other) absorption above 1100 nm. In the D6:C_{60} subcell, the undesired resonance is strongly reduced, due to its much weaker CT state absorption coefficient as compared to ZnPc:C_{60} in the 750–1100 nm range. Meanwhile, we also quantified the influence of the cross-talk by spectral rejection ratio (SRR), defined as the ratio of the external quantum efficiency (EQE) at the target response peak and the EQE at the cross-talk response peak. For the ZnPc:C_{60} subcell we find SRR on the order of 10^3, while for the D6:C_{60} subcell two order of magnitude lower SRR was achieved due to the strongly decreasing absorption with increasing wavelength, the calculation of SRR for our stacked OPDs are included in Tables S2 and S3, Supporting Information.

2.4. Achieving Independently Tunable Wavelengths over a Broad Spectral Range

The cavity thickness and resonance wavelength can be tuned by modifying the thickness of the absorber layer. In contrast to changing the cavity thickness by optimizing the transport layer thickness, this approach has the advantage that the increased path-length through the active layer enhances the light absorption, compensating for the relatively lower absorption coefficient at the wavelengths longer than 1100 nm.

Parasitic absorption of ETLs, HTLs and electrodes reduces the optical field maximum giving rise to a reduced photocurrent, the simulate device absorption can be found in Figure S3, Supporting Information. Therefore, the dopant concentration of the transport layers was optimized to reduce parasitic absorption, while simultaneously keeping ohmic contact and high charge carrier mobility. The employed HTL for both subcells is *N*,*N*,*N*′,*N*′-tetrakis(4-methoxyphenyl)-benzidine (MeO-TPD) lightly-doped (2 wt%) with 1,3,4,5,7,8-hexafluorotetracyanonaphthoquinodimethane (F6-TCNNQ). By decreasing the p-dopant concentration (F6-TCNNQ), MeO-TPD$^+$ and F6-TCNNQ$^-$ absorption in the wavelength range from 400 to 1600 nm decreases. Meanwhile, 2 wt% F6-TCNNQ is still sufficiently high to form an ohmic contact and provides sufficient conductivity for extracting holes.[23] Simultaneously, the ETL for both subcells is 4,7-diphenyl-1,10-phenanthroline (BPhen):Cesium (Cs) at 1:1 weight ratio which is often employed as ETL in organic solar cells and photodetectors.[24]

Figure 2 shows the experimentally achieved wavelength dependent EQEs of six OPDs in the dual stacked device architecture. By varying the cavity thicknesses, the respective resonance wavelengths in each of the subcells can be tuned independently. As shown in Figure 2a, when the thickness of D6:C_{60} layer is kept at 120 nm, varying the ZnPc:C_{60} layer thickness from 30 to 130 nm,[25] results in a peak shifting from 790 to 1180 nm. A maximum EQE of 16% is achieved at 790 nm with a 30 nm active layer. Due to its lower absorption coefficient at longer wavelengths, the cavity-enhanced EQE

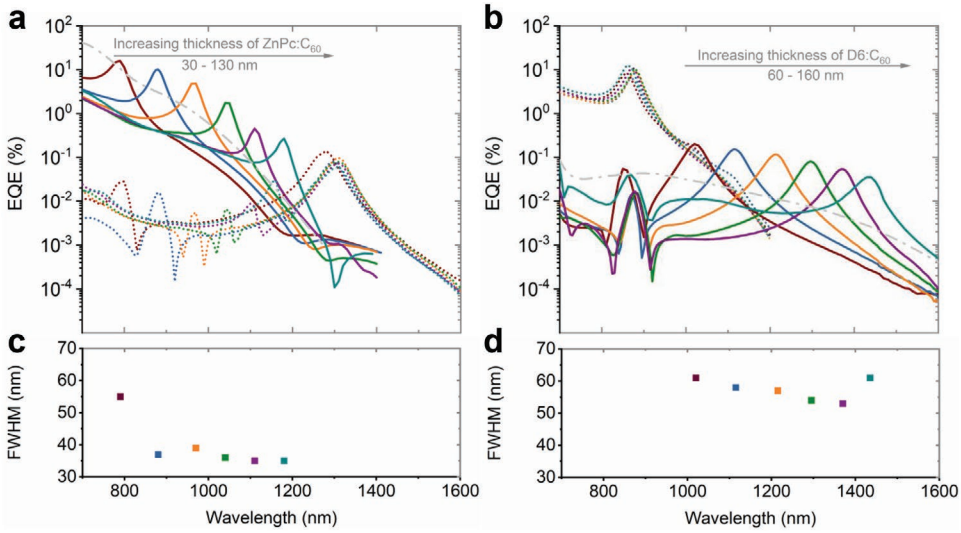

Figure 2. EQE spectra and corresponding FWHM of the stacked dual narrowband NIR OPDs. The resonance tunability is realized by varying the thickness of the photo-active layer in one subcell and keeping the other subcell thickness constant. a) By varying the thickness of ZnPc:C_{60} layer and keeping D6:C_{60} constant, the resonance wavelengths of ZnPc:C_{60} sub-photodetectors are tuned from 790 to 1180 nm, shown by solid lines. The dotted lines show the D6:C_{60} subcell. Whereas the dashed dotted gray line shows the EQE of a non-cavity ZnPc:C_{60} device. b) By varying the thickness of D6:C_{60} layer and keeping the other active layer constant, the resonance wavelengths of D6:C_{60} subcells cover the range of 1020–1435 nm, shown by solid lines. The dotted lines show the ZnPc:C_{60} subcell. Whereas the dashed dotted gray line shows the EQE of a non-cavity D6:C_{60} device. In both subfigures, the lower panel (c and d) depicts the FWHM for each device.

decreases. At 1180 nm, the EQE is 0.26% for a ZnPc:C_{60} active layer with a thickness of 130 nm. Nonetheless, compared with the non-cavity enhanced ZnPc:C_{60} device EQE, which is shown by dash-dotted line in Figure 2a, the weak CT state absorption at 1180 nm is enhanced up to 22 times through the use of the optical micro-cavity device architecture. Meanwhile, a narrow FWHM of 35 nm at response wavelength 1110 nm (Figure 2c) is achieved, indicating a high wavelength-detecting selectivity of the OPDs. While the resonance wavelength of the ZnPc:C_{60} sub-cavity could be varied over 390 nm from 790 to 1180 nm, the response peak of the D6:C_{60} sub-cavity shifts only 30 nm, from 1280 to 1310 nm, showing an almost independent tuning of the response wavelengths of the different sub-cavities.

For OPDs where the ZnPc:C_{60} layer thickness is kept at 50 nm and the D6:C_{60} thickness varied from 60 to160 nm, the D6:C_{60} subcell has resonance wavelengths from 1020 to 1435 nm with the response EQE decreasing from 0.21% to 0.035% (Figure 2b). As compared to the non-cavity device, shown by the dash-dotted line in Figure 2b, the EQE of the cavity-enhanced D6:C_{60} subcell is amplified up to 14 times, while FWHMs are in the range between 53 and 61 nm (Figure 2d). The small change of the response peak position from 860 to 880 nm of the ZnPc:C_{60} subcell once again proves that the response of the two sub-cavities can be tuned independently with minor influence on the other subcell.

2.5. Specific Detectivity D^*

In general, noise current (i_{noise}) is the sum of thermal, shot, 1/*f* and generation-recombination noise.[6] Shot noise only appears under applied bias. D^* of the stacked OPDs was measured under zero bias, and therefore, at sufficiently high frequencies thermal noise will be the dominant contributor to i_{noise}.[15,26] The specific detectivity D^* can be calculated using Equation (1)[27]

$$D^* = \frac{e\lambda A^{1/2}\mathrm{EQE}}{hcS_{th}} \quad (1)$$

where e is the elementary charge, λ the resonance wavelength, h Planck's constant and c the speed of light. The noise spectral density for thermal noise S_{th}, normalized by the device area A, can be obtained by Equation (2)

$$S_{th} = \sqrt{\frac{4k_BT}{R_{sh}}} \quad (2)$$

in which k_B is Boltzmann constant, T temperature and R_{sh} the shunt resistance.[28]

From the current–voltage characteristic (Figure S4, Supporting Information) we determine a shunt resistance of 10^5 and 10^4 Ω cm^2 at zero bias for the ZnPc:C_{60} and D6:C_{60} subcells, respectively. Despite varying the thickness of the active layers of the photodetectors, we find no dependence between photo-active layer thickness and shunt resistance. The specific detectivity D^* of most subcells is around 10^{11} Jones (ZnPc:C_{60}) in the spectral range 790–1180 nm and around 10^8 Jones (D6:C_{60}) in the range of 1020–1435 nm. Details on the calculation of D^* can be found in Table S4, Supporting Information. Both subcells have about one order lower D^* as compared to their single device counterparts which are fabricated in the same evaporation run (Table S4, Supporting Information). The relatively lower D^* of D6:C_{60} subcell is mainly due to the weaker resonance enhancement than that of the single photodetector: The D6:C_{60} sub-cavity is formed by two semi-transparent mirrors, while the single photodetector cavity is

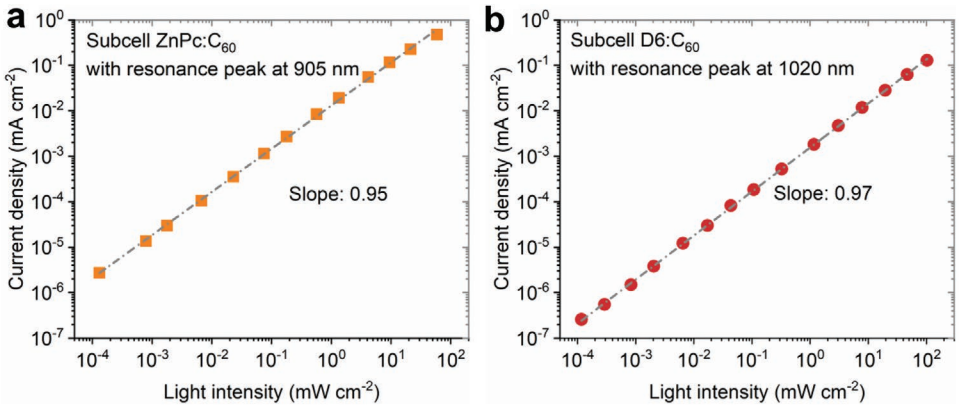

Figure 3. Linear dynamic range of ZnPc:C_{60} and D6:C_{60} subcells. Short-circuit current density versus light intensity for the a) ZnPc:C_{60} and b) D6:C_{60} subcell with resonance peak at 905 and 1029 nm, respectively.

formed by a semi-transparent and an opaque Ag mirror. The lower D^* of the ZnPc:C_{60} subcell can be explained by the fact that it is embedded below the D6:C_{60} subcell, which absorbs part of the light at the ZnPc:C_{60} subcell resonance wavelengths. Further details regarding the influence of Ag mirrors and active layer sequence on the resonance enhancement are presented in Figure S3, Supporting Information.

2.6. Linear Dynamic Range

The linear dynamic range (LDR) is defined as the linearity between light intensity and photocurrent in OPDs and is calculated via Equation (3)[1,6]

$$\mathrm{LDR} = 20 \log \frac{I_{\max}}{I_{\min}} \tag{3}$$

where the $I_{\max}$ and $I_{\min}$ are the maximum and minimum light intensity, in between which the photocurrent of the OPDs is linearly dependent on the light intensity. The LDR depicted in **Figure 3** is measured under zero bias using two different LEDs close to the resonance wavelengths, that is, 905 nm (ZnPc:C_{60}) and 1020 nm (D6:C_{60}), respectively. The ZnPc:C_{60} subcell (Figure 3a) has about six orders magnitude response linearity in the light intensity range of 10^{-4}–10^{2} mW cm^{-2}, which gives the LDR of 120 dB. When the light intensity exceeds 100 mW cm^{-2}, a deviation from linearity is observed, which indicates that bi-molecular recombination starts influencing the short-circuit current substantially.[29] D6:C_{60} sub-photodetector shows a stable linearity in an even broader light intensity range (10^{-4}–1.15×10^{2} mW cm^{-2}) (Figure 3b), corresponding to an LDR of 139 dB. The relatively high LDR for both of the subcells reveal that our stacked dual wavelength OPDs can be operated in a broad range of light intensities, comparable to its inorganic counterparts, making them a promising candidate for quantitative spectroscopy.[30]

2.7. Angular Dependence of the Spectral Response

The resonance enhancement in the cavity-based devices is the result of optical interference, which depends on the angle of incidence of the incoming light beam. **Figure 4** depicts the measured resonance peaks in the EQE spectrum for both subcells with resonance wavelengths at 965 nm (ZnPc:C_{60} subcell) and 1221 nm (D6:C_{60} subcell) as a function of the angle of incidence. Due to the dispersion of the cavity photons,[31] the resonance wavelengths blue-shift when incident angles deviating from normal incidence. Between 0° and 20°, the peak shift of ZnPc:C_{60} and D6:C_{60} subcells is not exceeding 15 and 20 nm, respectively, which is still smaller than the FWHM of both subcells (30 and 58 nm, respectively). For applications, one can adjust the light source perpendicular to the OPD and design the optical path such that one light is collected with an acceptance cone of ±10° or ±15°. In this way, spectroscopic features can be measured reliably.

2.8. Demonstration of a Compact Concentration Sensor

As a demonstration of an application of this dual wavelength OPD, we measure in the following the ethanol concentration in an ethanol/water solution. As presented in **Figure 5**a, water and ethanol have a large absorption contrast at both 980 and 1300 nm. In order to access those absorption regions, a device with resonant wavelength at 990 nm (ZnPc:C_{60}) and 1275 nm (D6:C_{60}) was employed, resulting in FWHMs of 39 and 53 nm, respectively.

A halogen lamp is used as light source, with an 850 nm long pass filter to filter out the above gap response. The ethanol concentration of six different solutions is determined by measuring the subcell signals. As shown in **Figure 6**, the linear relationship between ethanol concentration and device response current indicates a reliable assessment of both subcells. Typically, a single photodetector can only detect one wavelength of the measured samples, while the stacked dual wavelength OPDs provides more reliable measurements. Moreover, by sharing one detecting surface, these stacked OPDs have high potential to be used in ultracompact devices or images.

3. Conclusion

In summary, we present an ultra-compact organic three-terminal photodetector, which senses two specific NIR

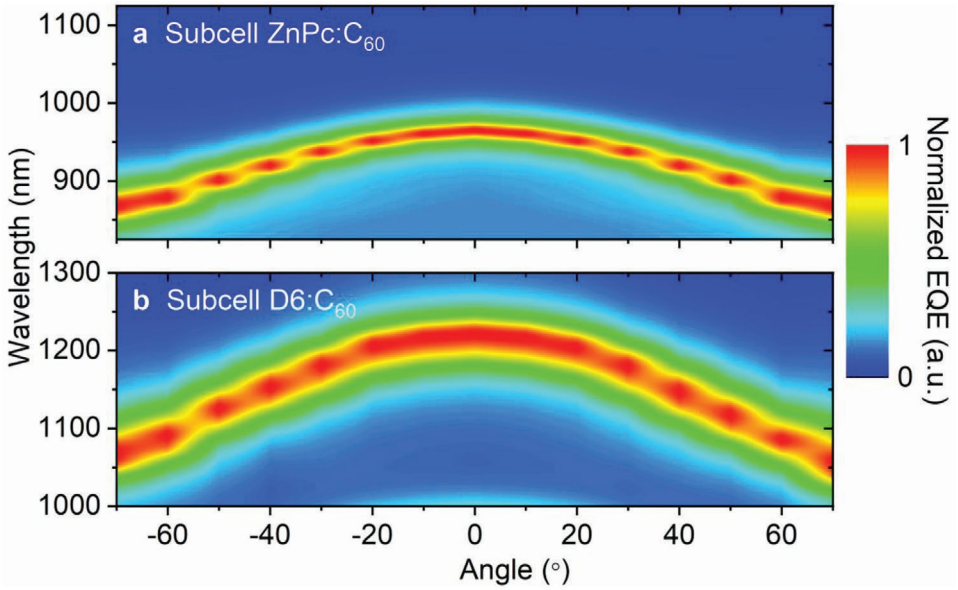

Figure 4. Incident light angular dependence property of cavity-based photodetectors. The resonance wavelength of a) ZnPc:C_{60} and b) D6:C_{60} subcells at normal incidence are 965 and 1221 nm, respectively.

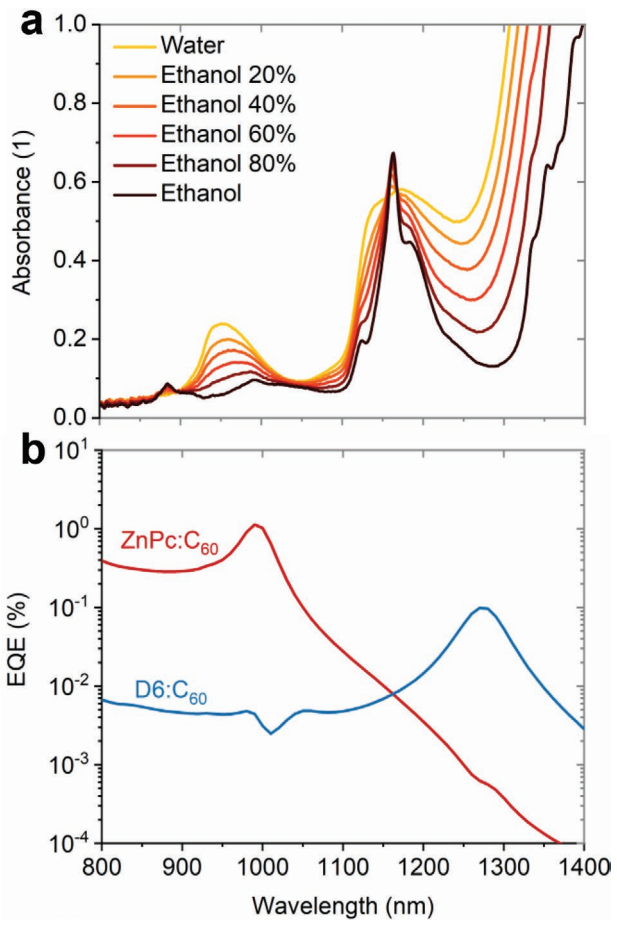

Figure 5. a) Absorbance of water and ethanol measured in a 10 mm cuvette thickness. b) EQE of ZnPc:C_{60} and D6:C_{60} subcells with resonance wavelength at 990 and 1275 nm, respectively.

wavelengths using a single detection area. For this purpose, two photodiodes are embedded in two stacked micro-cavities, where the first sub-cavity includes a semitransparent bottom and intermediate Ag mirror. Due to coherent coupling of both sub-cavities, a fraction of photons at the resonance wavelength of the first cavity is confined in the second sub-cavity. To minimize the resulting undesired resonance cross-talk, complementary CT state absorption and optimized cavity optics are used. The resonance wavelengths can be easily tuned, by varying the ZnPc:C60 and D6:C60 sub-cavity thicknesses and are in the range of 790–1180 nm and 1020–1435 nm with FWHMs as low as 35 and 61 nm. By selecting two wavelengths within these

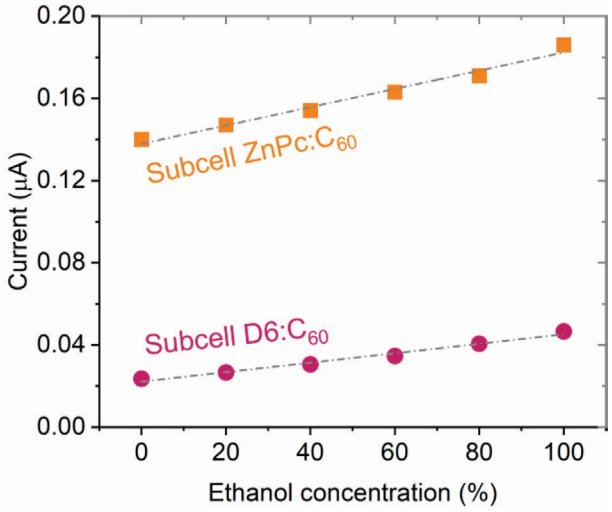

Figure 6. Concentration measurement of ethanol diluted in water. Orange squares (red dots) represent the current measured with the ZnPc:C_{60} (D6:C_{60}) subcell with the corresponding response peak at wavelength 990 nm (1275 nm).

ranges, we demonstrate the use of this sensor to determine the concentration of alcohol in a water solution.

To the best of our knowledge, this is the first demonstration of an organic dual narrow-band photodetector with high selectivity and broad range tunability. It is anticipated that this work can pave a way for highly integrated spectroscopic sensors based on dual wavelength OPDs with different combinations of photo-active materials for potential application in biomedicine, agriculture, and manufacturing industry.

4. Experimental Section

Device Fabrication: The stacked photodetectors were fabricated by thermal evaporation vacuum system (Kurt J. Lesker, UK) with base pressure less than 10^{-7} mbar. Devices layers were deposited on top of pre-cleaned glass substrates (Priz Optics, Germany). A series of shadow masks and mobile shutters were employed to control device layer configuration and thickness variation. To produce smooth Ag mirrors (electrodes), 3 nm MoO_3 and 1 nm Au were used as seed layers and deposited beneath the Ag mirrors (electrodes).[20] All involved organic materials underwent 2–3 sublimation before using. The area of the devices was 6.44 mm^2, being defined by the geometric intersection of the Ag electrodes. After fabricating, all of the devices were encapsulated with transparent glass by UV light curing epoxy resin (XNR 5592; Nagase ChemteX, Japan).

Device Characterization: The EQE measurement of the stacked NIR photodetectors was performed with a halogen lamp with power of 50 W. The light is chopped at 173 Hz and coupled into a monochromator (Newport Cornerstone 260 1/4m, USA). Two focal lenses were employed to focus the monochromatic light onto the detectors. To avoid the second harmonic of the light source, two long pass filters were used during the measurement of the photoresponse for wavelength longer than 800 nm. The devices were measured under short circuit condition and their current was magnified by a current–voltage preamplifier. A lock-in amplifier (Signal Recovery 7280 DSP, USA) with a time constant of 500 ms was used to measure the photocurrent. Calibrated silicon (Si) and an indium–gallium–arsenide (InGaAs) photodiode were used to measure the light intensity of the halogen lamp. The EQE was calculated by dividing the number of generated charges by the incoming photon flux.

Current–voltage (J–V) characteristic curves were measured with an SMU (2400 source meter, Keithley Instrument, USA) under ambient conditions. An AM1.5G sunlight simulator (16S-003-300-AM1.5 G sunlight simulator, Solar Light Co., USA) was employed as light source. The measured result was calibrated by a silicon photodiode (S1337 Hamamatsu-Photonics, Japan).

Linear Dynamic Range: A series of neutral density filters were used to vary the light intensity which was illuminated on the photodetectors. For light intensity lower than 0.2 mW cm^{-2} (wavelength 905 nm) and 0.02 mW cm^{-2} (wavelength 1020 nm), a xenon lamp combined with a monochromator were employed. The light was chopped at 173 Hz. The photocurrent was pre-amplified (10^{-5} A V^{-1}, Model 5182, Signal Recovery, USA) and analyzed by a lock-in amplifier (Model 7265, Signal Recovery, USA). For light intensity higher than 0.2 mW cm^{-2} (wavelength 905 nm) and 0.02 mW cm^{-2} (wavelength 1020 nm), two LEDs with illumination wavelength peak positions at 905 nm (H2W5-905, Roithner Lasertechnik, Germany) and 1020 nm (H2A1-H1020), respectively, were used as light sources. The photocurrent was measured under zero bias, recorded by a Keithley 2400 Source Meter and calibrated by a silicon photodiode (S1337 Hamamatsu-Photonics, Japan).

Angular Dependent EQE: Fourier-transform infrared spectroscopy (Nicolet Is50 FT-IR, USA) was used to measure angular dependent EQE. The measured devices were rotated every 10° step by a rotation mount. The light intensity of the FTIR was calibrated by Si and InGaAs photodiodes.

Absorbance of Ethanol and Water: The absorbance of ethanol and water was measured in a 10 mm thick cuvette by a two beams UV–vis–NIR spectrometer spectrophotometer (SolidSpec-3700i, Shimadzu Corporation, Japan).

Supporting Information

Supporting Information is available from the Wiley Online Library or from the author.

Acknowledgements

The authors acknowledge the DFG project VA 1035/5-1 (Photogen) and the Sächsische Aufbaubank through project no. 100325708 (InfraKart). The authors acknowledge Rico Meerheim and Paul Vince for fruitful discussions.

Open access funding enabled and organized by Projekt DEAL.

Conflict of Interest

The authors declare no conflict of interest.

Keywords

dual wavelength, micro-cavities, near infrared, organic photodetectors, tunable spectra

Received: October 15, 2020
Revised: November 20, 2020
Published online: December 28, 2020

[1] X. Gong, M. Tong, Y. Xia, W. Cai, J. S. Moon, Y. Cao, G. Yu, C.-L. Shieh, B. Nilsson, A. J. Heeger, *Science* **2009**, *325*, 1665.
[2] C. Lungenschmied, G. Dennler, H. Neugebauer, S. N. Sariciftci, M. Glatthaar, T. Meyer, A. Meyer, *Sol. Energy Mater. Sol. Cells* **2007**, *91*, 379.
[3] F. P. García De Arquer, A. Armin, P. Meredith, E. H. Sargent, *Nat. Rev. Mater.* **2017**, *2*, 16100.
[4] T. Rauch, M. Böberl, S. F. Tedde, J. Fürst, M. V. Kovalenko, G. Hesser, U. Lemmer, W. Heiss, O. Hayden, *Nat. Photonics* **2009**, *3*, 332.
[5] C. M. Lochner, Y. Khan, A. Pierre, A. C. Arias, *Nat. Commun.* **2014**, *5*, 5745.
[6] R. D. Jansen-van Vuuren, A. Armin, A. K. Pandey, P. L. Burn, P. Meredith, *Adv. Mater.* **2016**, *28*, 4766.
[7] T. Xu, Y. K. Wu, X. Luo, L. J. Guo, *Nat. Commun.* **2010**, *1*, 59.
[8] Y. Fang, Q. Dong, Y. Shao, Y. Yuan, J. Huang, *Nat. Photonics* **2015**, *9*, 679.
[9] W. Wang, F. Zhang, M. Du, L. Li, M. Zhang, K. Wang, Y. Wang, B. Hu, Y. Fang, J. Huang, *Nano Lett.* **2017**, *17*, 1995.
[10] Q. Lin, A. Armin, P. L. Burn, P. Meredith, *Nat. Photonics* **2015**, *9*, 687.
[11] D. M. Lyons, A. Armin, M. Stolterfoht, R. C. R. Nagiri, R. D. Jansen-Van Vuuren, B. N. Pal, P. L. Burn, S. C. Lo, P. Meredith, *Org. Electron.* **2014**, *15*, 2903.
[12] H. Zhang, S. Jenatsch, J. De Jonghe, F. Nuësch, R. Steim, A. C. Véron, R. Hany, *Sci. Rep.* **2015**, *5*, 9439.
[13] M. S. Ünlü, S. Strite, *J. Appl. Phys.* **1995**, *78*, 607.

[14] K. Vandewal, *Annu. Rev. Phys. Chem.* **2016**, *67*, 113.
[15] B. Siegmund, A. Mischok, J. Benduhn, O. Zeika, S. Ullbrich, F. Nehm, M. Böhm, D. Spoltore, H. Fröb, C. Körner, K. Leo, K. Vandewal, *Nat. Commun.* **2017**, *8*, 15421.
[16] Z. Tang, Z. Ma, A. Sánchez-Díaz, S. Ullbrich, Y. Liu, B. Siegmund, A. Mischok, K. Leo, M. Campoy-Quiles, W. Li, K. Vandewal, *Adv. Mater.* **2017**, *29*, 1702184.
[17] X. Tang, M. M. Ackerman, M. Chen, P. Guyot-Sionnest, *Nat. Photonics* **2019**, *13*, 277.
[18] Z. Lan, Y. Lei, W. K. E. Chan, S. Chen, D. Luo, F. Zhu, *Sci. Adv.* **2020**, *6*, eaaw8065.
[19] L. A. A. Pettersson, L. S. Roman, O. Inganäs, *J. Appl. Phys.* **1999**, *86*, 487.
[20] S. Schubert, J. Meiss, L. Müller-Meskamp, K. Leo, *Adv. Energy Mater.* **2013**, *3*, 438.
[21] K. Vandewal, J. Benduhn, V. C. Nikolis, *Sustainable Energy Fuels* **2018**, *2*, 538.
[22] C. Kaiser, K. S. Schellhammer, J. Benduhn, B. Siegmund, M. Tropiano, J. Kublitski, D. Spoltore, M. Panhans, O. Zeika, F. Ortmann, P. Meredith, A. Armin, K. Vandewal, *Chem. Mater.* **2019**, *31*, 9325.
[23] M. L. Tietze, J. Benduhn, P. Pahner, B. Nell, M. Schwarze, H. Kleemann, M. Krammer, K. Zojer, K. Vandewal, K. Leo, *Nat. Commun.* **2018**, *9*, 1182.
[24] K. Walzer, B. Maennig, M. Pfeiffer, K. Leo, *Chem. Rev.* **2007**, *107*, 1233.
[25] S. Ullbrich, B. Siegmund, A. Mischok, A. Hofacker, J. Benduhn, D. Spoltore, K. Vandewal, *J. Phys. Chem. Lett.* **2017**, *8*, 5621.
[26] Q. Li, Y. Guo, Y. Liu, *Chem. Mater.* **2019**, *31*, 6359.
[27] Y. Fang, A. Armin, P. Meredith, J. Huang, *Nat. Photonics* **2019**, *13*, 1.
[28] K. J. Baeg, M. Binda, D. Natali, M. Caironi, Y. Y. Noh, *Adv. Mater.* **2013**, *25*, 4267.
[29] G. Lakhwani, A. Rao, R. H. Friend, *Annu. Rev. Phys. Chem.* **2014**, *65*, 557.
[30] A. Armin, M. Hambsch, I. K. Kim, P. L. Burn, P. Meredith, E. B. Namdas, *Laser Photonics Rev.* **2014**, *8*, 924.
[31] G. Panzarini, L. C. Andreani, A. Armitage, D. Baxter, M. S. Skolnick, V. N. Astratov, J. S. Roberts, A. V. Kavokin, M. R. Vladimirova, M. A. Kaliteevski, *Phys. Solid State* **1999**, *41*, 8.